WILEY | Hindawi

Research Article

Correction of Misalignment Errors in the Integrated GNSS and Accelerometer System for Structural Displacement Monitoring

Xuanyu Qu [iD],[1,2] Xiaoli Ding [iD],[1,2] You-Lin Xu [iD],[3] and Wenkun Yu [iD][4]

[1]*Department of Land Surveying and Geo-Informatics, The Hong Kong Polytechnic University, Hong Kong, China*
[2]*Research Institute for Land and Space, The Hong Kong Polytechnic University, Hong Kong, China*
[3]*School of Civil Engineering, Southwest Jiaotong University, Chengdu 610036, China*
[4]*School of Geosciences and Info-Physics, Central South University, Changsha 410083, China*

Correspondence should be addressed to Xiaoli Ding; xl.ding@polyu.edu.hk

Structural health monitoring (SHM) systems are widely deployed to monitor the dynamic behaviors of large civil infrastructures such as bridges and tall buildings. Global Navigation Satellite System- (GNSS-) based technologies are often a key component in such an SHM system considering the unique capability of GNSS in determining real-time displacements. GNSS often integrates with an accelerometer to achieve complementary advantages. However, due to the various error sources in GNSS measurements and accelerometer, accuracies of GNSS and accelerometer fusion results often cannot meet the requirements of SHM. We propose to integrate a multi-antenna GNSS and an accelerometer with an unscented multi-rate Kalman filter (UMRKF-MA) to correct the system misalignment errors between the sensors, aiming to produce a much more accurate real-time displacement measurement technology for monitoring large civil infrastructures. Extensive experiments with datasets gathered using a shaking table have indicated that the proposed method was able to improve the accuracy of real-time displacement measurements by up to about 40–65% compared to some existing approaches, and that a 1 mm level of real-time monitoring of displacements could be achieved with the method. The method has also been applied to process a dataset from a real-world long-span bridge when heavy vehicles passed through the bridge in a loading test and significantly improved results were obtained.

1. Introduction

Civil engineering structures such as buildings, long-span bridges, elevated roads, and dams play critical roles in supporting the daily lives of urban residents. Aging and wearing of the structures may lead to structural failures, resulting in financial and life losses. For example, the Sampoong Department Store in Seoul, South Korea, collapsed on 29th June 1995 and resulted in the loss of over 500 lives [1]. It is vital in many cases to deploy a structural health monitoring (SHM) system to detect structural defects and to warn of pending risks of structural failure.

Global Navigation Satellite System (GNSS) has become an effective technology for structural health monitoring [2–5]. The technology has a unique advantage in obtaining real-time three-dimensional displacements of a structure [6, 7]. The accuracy of the GNSS-based technology is however often unable to meet the requirements of structural health monitoring [8]. GNSS measurements are generally noisier than most other sensors such as accelerometers, survey total stations, and transducers [9]. Additionally, the data sampling rate of GNSS is often lower relatively [10, 11].

GNSS technology has been commonly integrated with other sensors considering the complementary natures of the sensors to improve the overall performance of the fusion systems [12, 13]. For example, GNSS and accelerometers have been integrated in many cases [14, 15] in both post-processing mode using, e.g., empirical mode decomposition- (EMD-) based [16] or digital filter-based fusion method [17, 18, 19], and real-time mode using, e.g., multi-rate Kalman filter (MRKF) [20–24]. Paziewski et al. [25] integrated

accelerometer measurements and displacements derived from asynchronous GNSS observations to detect the dynamic displacements.

Systematic errors may occur when using a standard Kalman filter to deal with nonlinear states, e.g., earthquake-induced vibrations [26]. An unscented Kalman filter has been proposed to model the nonlinear effects in navigation applications [27, 28]. In addition, very limited studies have addressed errors caused by the misalignment between the coordinate frames of GNSS and accelerometers (referred to as misalignment errors hereafter) in an SHM system. The coordinate frame of the GNSS is fixed in space while that of the accelerometer is not, and it varies with the attitude of the structural element that the accelerometer is attached on. Therefore, the three axes of the accelerometer are normally not aligned well with those of the GNSS even though both instruments are attached to the same structural element. The errors become especially significant when the structure rotates due to, e.g., strong winds and heavy vehicle load. The errors can therefore significantly affect the results of the data fusion. A high-pass filter can be adopted considering the fact that the misalignment errors usually exhibit low-frequency characteristics [31, 32]. The technique however may lead to the loss of some useful low-frequency displacement information [31].

Since the misalignment error is caused by the tilt of the structural element, it is theoretically possible to eliminate this misalignment error by determining the rotation angles of a structure. Two different frames can be connected by rotation in the direction of the coordinate axis [32]. Although a gyroscope can be adopted to record the rotation angles in real time, this has rarely been done in practice possibly due to reasons such as additional equipment cost. In this study, we address the misalignment problem in the integrated GNSS and accelerometer system using a multi-antenna (MA) GNSS that is capable of recording the precise attitude information of a structure. Typical applications of an MA-GNSS for attitude determination have been repeatedly demonstrated over the years in, e.g., marine surveying, navigation (e.g., cruise, vehicle, and drones), and seismology [33], but have been rarely considered in an SHM system. Furthermore, the known geometry of an MA-GNSS can be used as a constraint to improve attitude and positioning accuracy (i.e., precision single point positioning (PPP) and relative positioning). For example, Wu et al. [34] proposed a relative positioning model for an MA-GNSS to improve the ambiguity fixing rate and the accuracy of positioning.

We propose a new method that jointly uses a multi-antenna GNSS (MA-GNSS), an accelerometer, and an unscented multi-rate Kalman filter (UMRKF) for correcting the system misalignment errors and for high-accuracy dynamic structural displacement monitoring. The method also eliminates potential nonlinear systematic errors in the

system. Data generated with a shaking table that simulates both random and sinusoidal displacements and from a large cable-stayed bridge in Hong Kong during a loading test will be used to validate the effectiveness of the proposed method.

2. Methodology

A multi-antenna GNSS and an accelerometer are combined in this study to achieve high-accuracy displacement measurement of civil infrastructures. The multi-antenna GNSS is deployed to obtain precise displacement and attitude information of a structure where the known distances between the GNSS antennas are used as constraints in the GNSS solutions. A prototype of such an MA-GNSS is given in Section 3.1. The attitude information is used to correct the misalignment error of the accelerometer. The corrected acceleration measurements will then be fused with the displacement measurements derived with the MA-GNSS by the UMRKF to improve displacement measurements.

2.1. Multi-Rate Kalman Filter. The three-dimensional (3D) displacement measurements from the GNSS and the acceleration measurements from the accelerometer data are fused with the multi-rate Kalman filter. Since the sampling rate of the accelerometer is typically much higher than that of the GNSS, the multi-rate Kalman filter updates the state parameters at the data sampling rate of the accelerometer while the GNSS measurements are only used when a new epoch of GNSS measurements is available [20]. The state vector x_k of the Kalman filter is

$$x_k = \begin{bmatrix} d_k & \dot{d}_k \end{bmatrix}^T, \tag{1}$$

where d_k and $\dot{d}_k$ are the 3D displacement and velocity vectors of a monitoring point, respectively. The dynamic system state is written as [20]

$$x_k = \phi_{k-1} x_{k-1} + \psi_{k-1} u_{k-1} + w_{k-1}, \tag{2}$$

where ϕ_{k-1} is the transition matrix of the state vector and ψ_{k-1} is a design matrix, defined as

$$\phi_{k-1} = \begin{bmatrix} I_{3\times3} & \tau_a \cdot I_{3\times3} \\ 0_{3\times3} & I_{3\times3} \end{bmatrix},$$

$$\psi_{k-1} = \begin{bmatrix} 0.5 \cdot \tau_a^2 \cdot I_{3\times3} \\ \tau_a \cdot I_{3\times3} \end{bmatrix}, \tag{3}$$

where $I_{3\times3}$ and $0_{3\times3}$ are the 3×3 identity and zero matrices, respectively, and τ_a is the sampling interval of the accelerometer data. u_{k-1} is the vector of 3D accelerations; w_{k-1} is the noise matrix.

$$u_{k-1} = \begin{bmatrix} a_x & a_y & a_z \end{bmatrix}^T, w_{k-1} \sim N(0, Q_{k-1}), \tag{4}$$

where Q_{k-1} is the covariance matrix of the predicted states, which can be written as

$$Q_{k-1} = \begin{bmatrix} \dfrac{\tau_a^3}{3q} & 0 & 0 & \dfrac{\tau_a^2}{2q} & 0 & 0 \\ 0 & \dfrac{\tau_a^3}{3q} & 0 & 0 & \dfrac{\tau_a^2}{2q} & 0 \\ 0 & 0 & \dfrac{\tau_a^3}{3q} & 0 & 0 & \dfrac{\tau_a^2}{2q} \\ \dfrac{\tau_a^2}{2q} & 0 & 0 & \dfrac{\tau_a}{q} & 0 & 0 \\ 0 & \dfrac{\tau_a^2}{2q} & 0 & 0 & \dfrac{\tau_a}{q} & 0 \\ 0 & 0 & \dfrac{\tau_a^2}{2q} & 0 & 0 & \dfrac{\tau_a}{q} \end{bmatrix}, \quad (5)$$

where q is the noise factor of the acceleration measurements.

The observation equation of the MRKF is

$$L_k = H_{k-1}x_{k-1} + e_{k-1}, e_{k-1} \sim (0, R_{k-1}),$$
$$H_{k-1} = \begin{bmatrix} I_{3\times3} & 0_{3\times3} \end{bmatrix}, \quad (6)$$

where L_k is the vector of observations that contains the 3D displacements from the GNSS observations; H_{k-1} is the design matrix; and R_{k-1} is the variance-covariance matrix of the observations and defined as

$$R_{k-1} = \begin{bmatrix} \dfrac{r}{\tau_a} & \dfrac{r}{\tau_a} & \dfrac{r}{\tau_a} \end{bmatrix}^T, \quad (7)$$

where r is the noise factor of the GNSS displacement measurements in an SHM system.

2.2. Unscented Multi-Rate Kalman Filter.

The unscented multi-rate Kalman filter (UMRKF) is a variation of the MRKF that considers nonlinear state estimation based on the use of the unscented Kalman filter (UKF) [35]. For epoch k, a nonlinear state system consisting of random variables x_k with white Gaussian noise w_k and observations Z_k with white Gaussian noise e_k can be described as

$$\begin{cases} x_k = f(x_{k-1}, w_{k-1}), \\ Z_k = h(x_{k-1}, e_{k-1}), \end{cases} \quad (8)$$

where f is the nonlinear state transition equation and h is the nonlinear observation equation. The steps of the UKF algorithm for estimating the n-dimensional state vector x at

time k are as follows. First, $2n + 1$ sample points (sigma point set) are obtained first based on the unscented transformation (UT). Second, the predicted state vector $\overline{x}_k$ and its covariance matrix $P_{\overline{x}_k}$ are then calculated [27]:

$$(\tilde{x}_k)_i = f[(\tilde{x}_{k-1})_i], i = 1, 2, \cdots, 2n + 1,$$
$$\overline{x}_k = \sum_{i=1}^{2n+1} \omega_i (\tilde{x}_k)_i,$$
$$P_{\overline{x}_k} = P_{\omega_{k-1}} + \sum_{i=1}^{2n+1} \omega_i [(\tilde{x}_k)_i - \overline{x}_k][(\tilde{x}_k)_i - \overline{x}_k]^T, \quad (9)$$

where $(\tilde{x}_k)_i$ is the ith sigma point of the state vector and ω_i is the weight of the sigma point. Third, the predicted observation vector $\overline{L}_k$ and its covariance $P_{\overline{L}_k}$ as well as the cross-covariance matrix $P_{\overline{x}_k\overline{L}_k}$ are calculated:

$$(\tilde{L}_k)_i = h[(\tilde{x}_{k-1})_i], i = 1, 2, \cdots, 2n + 1,$$
$$\overline{L}_k = \sum_{i=1}^{2n+1} \omega_i (\tilde{L}_k)_i,$$
$$P_{\overline{L}_k} = P_{k-1} + \sum_{i=1}^{2n+1} \omega_i [(\tilde{L}_k)_i - \overline{L}_k][(\tilde{L}_k)_i - \overline{L}_k]^T, \quad (10)$$
$$P_{\overline{x}_k\overline{L}_k} = P_{k-1} + \sum_{i=1}^{2n+1} \omega_i [(\tilde{x}_k)_i - \overline{x}_k][(\tilde{L}_k)_i - \overline{L}_k]^T,$$

where $(\tilde{L}_k)_i$ is the ith sigma point of the predicted observation vector and $\overline{L}_k$ is the weighted mean of the observation vector. Finally, the estimated state vector $\hat{x}_k$, its covariance $P_{\hat{x}_k}$, and the UKF gain matrix K_k can be updated as [35]

$$\hat{x}_k = \overline{x}_k + K_k(L_k - \overline{L}_k),$$
$$P_{\hat{x}_k} = P_{\overline{x}_k} - K_k P_{\overline{L}_k} K_k^T, \quad (11)$$
$$K_k = \frac{P_{\overline{x}_k\overline{L}_k}}{P_{\overline{L}_k}}.$$

2.3. Correction of Misalignment Errors Based on Multi-Antenna GNSS Observations.

Figure 1 shows the two coordinate frames, i.e., the bridge reference frame (BRF, $O - x^b y^b z^b$) and the accelerometer reference frame (ARF, $O - x^a y^a z^a$). The former is defined according to the bridge geometry (x^b being horizontal and in the direction of the bridge alignment, y^b being horizontal and perpendicular to x^b, and z^b in the vertical direction) while the latter refers to a coordinate system as defined by the three axes of the accelerometer. In general, the two coordinate frames are aligned. However, when the accelerometer experiences tilting or torsion, the ARF changes to $O - x^{a'} y^{a'} z^{a'}$.

We define the rotation angles around the y-, x-, and z-axes as pitch (p), roll (r), and yaw (y), respectively. $\begin{bmatrix} p & r & y \end{bmatrix}^T$ are connected to the BRF and the ARF:
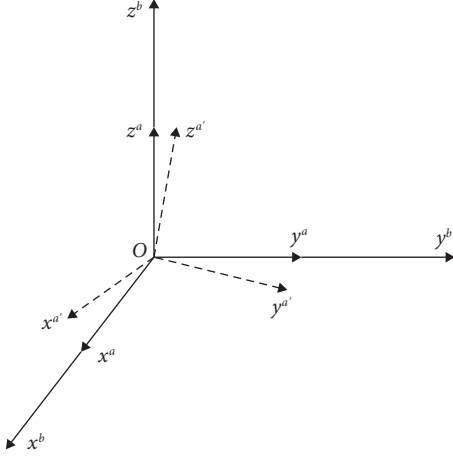
FIGURE 1: Accelerometer body frame (x^a, y^a, z^a) and bridge reference frame (x^b, y^b, z^b).

$$
\begin{bmatrix} x_a \\ y_a \\ z_a \end{bmatrix} = C_b^a \begin{bmatrix} x_b \\ y_b \\ z_b \end{bmatrix}, \tag{12}
$$

$$
C_b^a = \begin{bmatrix} C_r C_y - S_r S_p S_y & C_r S_y + S_r S_p S_y & -S_r C_p \\ -C_p S_y & C_p C_y & S_y \\ S_r C_y + C_r S_p S_y & S_r S_y - C_r S_p C_y & C_r C_p \end{bmatrix}, \tag{13}
$$

where $\begin{bmatrix} x_a & y_a & z_a \end{bmatrix}^T$ and $\begin{bmatrix} x_b & y_b & z_b \end{bmatrix}^T$ denote the 3D displacements in x-, y- and z-directions, respectively. The subscripts a and b represent the ARF and BRF, respectively. C_b^a is an orthogonal transformation matrix. $C_b^{a-1} = C_b^{aT} = C_a^b$. $C(\cdot)$ and $S(\cdot)$ are cosine and sine operators, respectively. In general, the rotation angles of a civil engineering structure are small. Therefore equation (13) can be replaced with

$$
C_a^b = C_b^{aT} \approx \begin{bmatrix} 1 & -y & r \\ y & 1 & -p \\ -r & p & 1 \end{bmatrix}. \tag{14}
$$

Equation (12) can then be written as

$$
\begin{bmatrix} x_b \\ y_b \\ z_b \end{bmatrix} = C_a^b \begin{bmatrix} x_a \\ y_a \\ z_a \end{bmatrix} = \begin{bmatrix} 1 & -y & r \\ y & 1 & -p \\ -r & p & 1 \end{bmatrix} \begin{bmatrix} x_a \\ y_a \\ z_a \end{bmatrix}. \tag{15}
$$

We assume that the ARF and BRF of an SHM system are initially in fine alignment. The accelerometer data can be converted from ARF to BRF and integrated with the GNSS measurements based on equations (12)–(15). The observation equation for the acceleration measurements can then be obtained as shown in the following equation [14, 31]:

$$
\begin{bmatrix} a_x' , \\ a_y' , \\ a_z' - g. \end{bmatrix}_k = \begin{bmatrix} 1 & -y & r \\ y & 1 & -p \\ -r & p & 1 \end{bmatrix}_k \begin{bmatrix} a_x \\ a_y \\ a_z - g. \end{bmatrix}_k + \begin{bmatrix} \varepsilon_x \\ \varepsilon_y , \\ \varepsilon_z \end{bmatrix}_k, \tag{16}
$$

$$
\begin{bmatrix} a_x' , \\ a_y' , \\ a_z' . \end{bmatrix}_k = \begin{bmatrix} a_x \\ a_y \\ a_z \end{bmatrix}_k + \begin{bmatrix} \varepsilon_x \\ \varepsilon_y \\ \varepsilon_z \end{bmatrix}_k
$$
$$
+ \begin{bmatrix} 0 & g - a_z & a_y \\ a_z - g & 0 & -a_x \\ -a_y & a_x & 0 \end{bmatrix}_k \begin{bmatrix} p \\ r \\ y \end{bmatrix}_k, \tag{17}
$$

where, $\begin{bmatrix} a_x' & a_y' & a_z' \end{bmatrix}^T$ and $\begin{bmatrix} a_x & a_y & a_z \end{bmatrix}^T$ denote the 3D acceleration measurements in the BRF and ARF, respectively. $\begin{bmatrix} \varepsilon_x & \varepsilon_y & \varepsilon_z \end{bmatrix}_k^T$ is the vector of acceleration residuals that are assumed to be zero-mean white Gaussian noise. g is the acceleration due to gravity.

It can be seen from the above discussion that rotation angles $\begin{bmatrix} p & r & y \end{bmatrix}^T$ are needed to calculate the 3D accelerations in the BRF. We propose to use a multi-antenna GNSS to determine the rotation angles. Rotation matrix C_a^b (see equation (15)) can be estimated based on the least squares principle [36]:

$$
\min : \sum_{i=1}^m W_i \left\| B_i - C_a^b \bullet A_i \right\|^2, \tag{18}
$$

where $B_i = \begin{bmatrix} x_{b,i} & y_{b,i} & z_{b,i} \end{bmatrix}^T$ and $A_i = \begin{bmatrix} x_{a,i} & y_{a,i} & z_{a,i} \end{bmatrix}^T$ are the coordinates of the ith GNSS antenna in the BRF and ARF, respectively, $i = 1, 2, \ldots, m$ represents the number of a GNSS antenna, and W_i is a positive weighting parameter.

2.4. Integration of Multi-Antenna GNSS and Accelerometer Measurements Based on UMRKF. The UMRKF is used to fuse the multi-antenna GNSS and accelerometer measurements to achieve high-accuracy measurements of displacements. The state vector x_k in equation (1) is first extended into the following:

$$
x_k = \begin{bmatrix} d_x & d_y & d_z & \dot{d}_x & \dot{d}_y & \dot{d}_z & p & r & y \end{bmatrix}^T, \tag{19}
$$

where $\begin{bmatrix} d_x & d_y & d_z \end{bmatrix}^T$, $\begin{bmatrix} \dot{d}_x & \dot{d}_y & \dot{d}_z \end{bmatrix}^T$, and $\begin{bmatrix} p & r & y \end{bmatrix}^T$ are the displacements, velocities, and rotation angles about x-, y-, and z-axes, respectively. The transition matrices ϕ_{k-1} and ψ_{k-1} in equation (2) accordingly become

$$
\phi_{k-1} = \begin{bmatrix} I_{3\times3} & \tau_a \cdot I_{3\times3} & 0_{3\times3} \\ 0_{3\times3} & I_{3\times3} & 0_{3\times3} \\ 0_{3\times3} & 0_{3\times3} & I_{3\times3} \end{bmatrix},
$$
$$
\psi_{k-1} = \begin{bmatrix} 0.5 \cdot \tau_a^2 \cdot I_{3\times3} \\ \tau_a \cdot I_{3\times3} \\ 0_{3\times3} \end{bmatrix}, \tag{20}
$$

where $I_{3\times3}$ and $0_{3\times3}$ are 3×3 identity and zero matrices, respectively; we assume that the rotation angles vary over time and behave as random-walk variables:

$$\begin{bmatrix} p \\ r \\ y \end{bmatrix}_k = \begin{bmatrix} p \\ r \\ y \end{bmatrix}_{k-1} + \begin{bmatrix} \varepsilon_p \\ \varepsilon_r \\ \varepsilon_y \end{bmatrix}, \quad (21)$$

where $\begin{bmatrix} \varepsilon_p & \varepsilon_r & \varepsilon_y \end{bmatrix}^T$ denote the process noise. The observations from the MA-GNSS and the observation matrix are

$$z_k = \begin{bmatrix} d_x & d_y & d_z & p & r & y \end{bmatrix}^T, \quad (22)$$

$$H_{k-1} = \begin{bmatrix} I_{3\times3} & 0_{3\times3} & 0_{3\times3} \\ 0_{3\times3} & 0_{3\times3} & I_{3\times3} \end{bmatrix}, \quad (23)$$

where z_k is the observation from the MA-GNSS including the 3D displacements and three Euler angles and H_{k-1} is the design matrix. The overall framework of the proposed method is shown in Figure 2.

3. Experiments with Data from a Shaking Table

3.1. Experimental Setup. Several simulation tests were investigated using a shaking table set up on the terrace garden of Block Z on the campus of the Hong Kong Polytechnic University. As shown in Figure 3, a shaking table was used with a four-antenna GNSS (Trimble R12 and Leica GR25) and a MEMS (micro-electromechanical system) accelerometer (model: TE Connectivity 4630a-005) to simulate and record the displacements. The shaking table was capable of generating several types of displacements in horizontal direction with a peak-to-peak displacement range of 150 mm. To record the actual displacements of the shaking table, a laser transducer (model: Keyence LK-503) was deployed parallel to the shaking direction of the shaking table, and a signal reflector was fixed on the shaking table edge to obtain the high-accuracy (0.01 mm) displacements of the shaking table.

The MA-GNSS consisted of two sets of Trimble R12 geodetic receivers (ANT2 and ANT3 in Figure 3(a)), one set of Leica GR25 GNSS geodetic receivers (ANT1 in Figure 3(a)), and one set of on-board Septentrio GNSS receiver (ANT4 in Figure 3(a)). The distances between ANT1, ANT2, and ANT3 were 1.2 m and antenna ANT4 was mounted on the center. The GNSS antennas were mounted on a rigid triangular platform. All the other sensors used in the study were synchronized to the GPS time. The ARF of the accelerometer was initially aligned with the BRF and is shown in Figure 3(a) (blue lines). The GNSS reference station (model: Trimble Net R9) was set up about 50 m away from the shaking table to provide correction information.

The dynamic response of a structure induced by different loadings, e.g., temperature, crossing winds, traffic flows, and earthquakes, may exhibit different waveforms [37]. Two typical types of displacement signals were simulated in the experiments, i.e., a random signal and a 1 Hz sinusoidal signal with an amplitude of 1.9 cm. The displacements
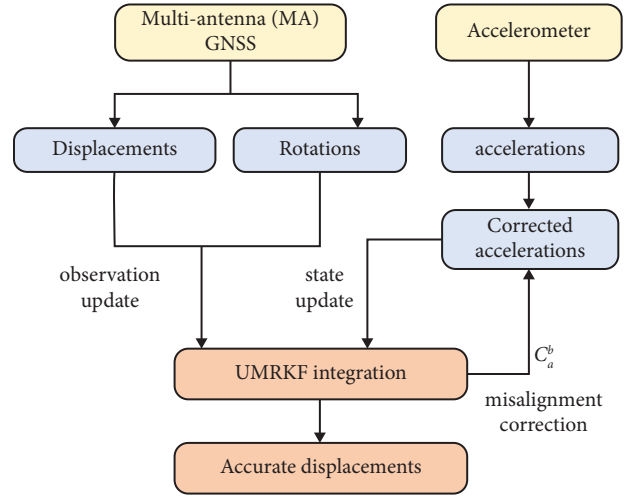

Figure 2: Framework of the proposed method for integrated use of multi-antenna GNSS and accelerometer observations.

simulated by the shaking table were measured by the MA-GNSS, the accelerometer, and the laser transducer, with the sampling rate of 20 Hz, 200 Hz, and 200 Hz, respectively. A GNSS reference station was set up on the roof top of the same building to enable RTK (real-time kinematic) GNSS data processing. The details of RTK parameters are shown in Table 1.

In the experiments, the shaking table was first kept static to obtain the reference coordinates. The motion signals were then uploaded onto the shaking table system. The shaking table was tilted for some small angles in the northwest direction by manually adjusting one of the leveling screws located on the corner of the platform to generate the misalignment errors. The tilt angle of the platform was first raised slowly to a certain angle (less than 2°) and then lowered until it was close to the initial level. Six calculated schemes were used for comparison:

> Scheme 1: displacements from GNSS observations only
>
> Scheme 2: displacements from accelerometer measurements by double integration after a high-pass filter
>
> Scheme 3: displacements from GNSS and accelerometer data fusion based on the EMD model (EMD hereafter) proposed by Chan et al. [16]
>
> Scheme 4: displacements from GNSS and accelerometer data fusion based on conventional MRKF (CMRKF)
>
> Scheme 5: displacements from multi-antenna GNSS and accelerometer data fusion based on conventional MRKF (CMRKF-MA)
>
> Scheme 6: displacements from multi-antenna GNSS and accelerometer data fusion based on unscented MRKF (UMRKF-MA)

It should be noted that as demonstrated in Chan et al. [16], to obtain the fusion results using Scheme 3, another static GNSS monitoring station is needed to mitigate the
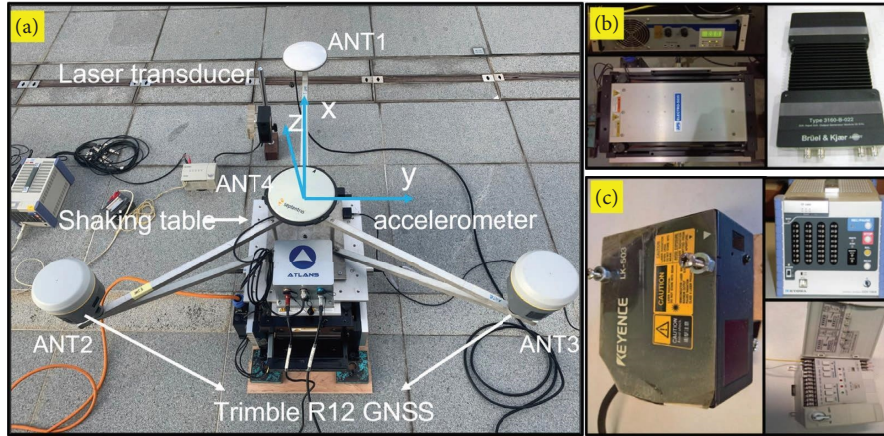
FIGURE 3: Experimental setup for simulating and recording various types of displacements. (a) Shaking table with a multi-antenna GNSS and an accelerometer and the bridge reference frame (blue lines). (b) Shaking table signal generator. (c) Laser transducer.

TABLE 1: Key parameters of GNSS RTK positioning.

Parameter	Settings
Observations	Double-differenced dual-frequency carrier-phase and pseudorange (GPS L1 and L2), Galileo E1 and E5A, and BDS (B1 and B2)
Cutoff angle	12°
Observation weighting scheme	An elevation-dependent scheme based on the cosecant function
Baseline length	About 100 m
Estimation method	Kalman filter
Antenna phase center offsets	Corrected with Antex igs14.atx [38]
Atmospheric delays	Eliminated in double-differencing
Ambiguity	Estimated and fixed to integers with Lambda

background noise of the GNSS. In this study, a high-pass Butterworth filter [39] is only applied in Scheme 2, with a cutoff frequency of 0.05 Hz to mitigate the low-frequency effects.

3.2. Experiment with Sinusoidal Displacements.

Sinusoidal displacements in the horizontal direction were simulated by the shaking table and recorded by the MA-GNSS, the accelerometer (ACC), and the laser transducer (True). Displacements were then calculated based on the six computational schemes mentioned above. The displacements from the GNSS data only and the EMD fusion solutions were 20 Hz and those from the other four solutions were 200 Hz. The calculated displacements were compared with the laser measurements (black lines and used as the truth). The errors in the displacements, i.e., differences between the laser measurements and the calculated displacements from the six computation schemes, are shown in Figure 4 where the errors (blue lines) were shifted by -5 cm for visualization clarity. The RMSE (root-mean-square error) and the peak errors were calculated to evaluate the performances of the different methods as shown in Table 2.

As shown in Figure 4, the displacements could be captured by all the methods except for using only the ACC measurements. The GNSS data-only solutions (Figure 4(a)) had a good agreement with the laser measurements, and the RMSE and peak error were 1.5 mm and 4.2 mm, respectively.

There was a systematic shift in the ACC solutions (Figure 4(b)) for the period of sinusoidal displacements (about 65 s to 200 s), resulting in RMSE and peak errors of 8.1 mm and 18.3 mm, respectively. This can be attributed to the misalignment errors induced by tilting the shaking table. The EMD results (Figure 4(c)) achieved an RMSE of 1.4 mm. The possible reason for the good performance was that the misalignment errors were filtered out in the denoising process. However, the EMD fusion algorithm requires an additional high-precision GNSS observation station nearby to eliminate the environmental noise (e.g., multi-path), which makes this algorithm impossible for online processing.

The displacements derived with CMRKF (Figure 4(d)) were significantly contaminated by the misalignment errors, resulting in a systematic shift with the RMSE being 2.5 mm. The proposed technique effectively mitigated the impact of the misalignment errors (Figures 4(e) and 4(f)). The UMRKF-MA solutions achieved the best performance, with the RMSE and the peak error lowered to 1.0 mm and 2.5 mm, respectively.

Welch's power spectral density (PSD) [40] of the displacements from the different computational schemes and laser measurements are shown in Figure 5. For the low-frequency band (0.01–0.2 Hz, zone 1), comparable PSD results can be observed among the different solutions and the laser measurements, except for the ACC solutions that deviated more from the other results. All the methods could
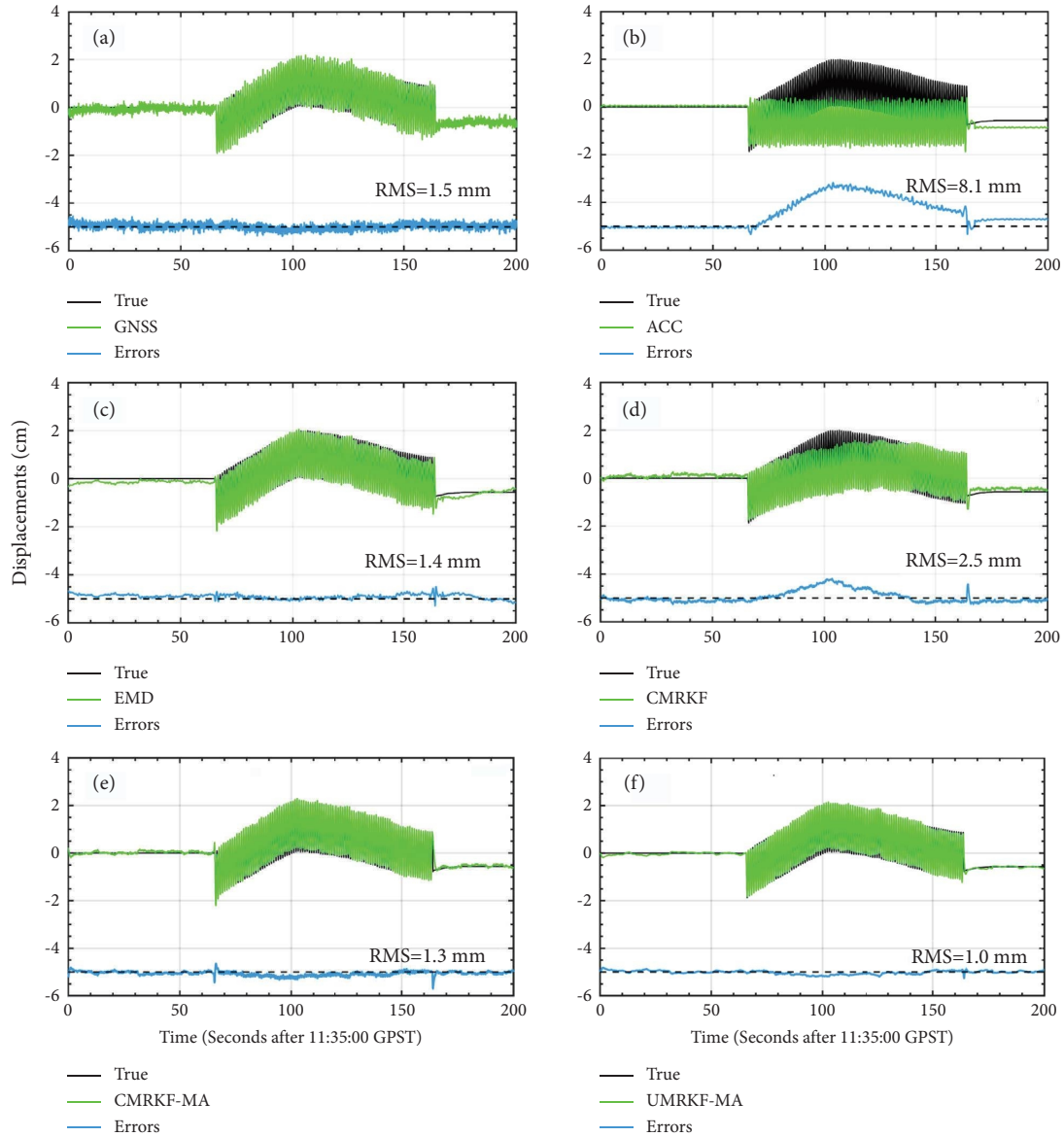
FIGURE 4: Displacement solutions and their errors for the test with simulated sinusoidal displacements. (a) GNSS data only. (b) Accelerometer data only after a high-pass filter. (c) GNSS and accelerometer data fusion with EMD. (d) GNSS and accelerometer data fusion with CMRKF. (e) GNSS and accelerometer data fusion with CMRKF-MA. (f) GNSS and accelerometer data fusion with UMRKF-MA.

TABLE 2: Statistics of errors of different solutions (unit: mm).

Computation schemes	GNSS	ACC	EMD	CMRKF	CMRKF-MA	UMRKF-MA
Peak error	4.2	18.3	5.0	8.2	7.0	2.5
RMSE	1.5	8.1	1.4	2.5	1.3	1.0

capture the 1 Hz sinusoidal displacements accurately. When the frequency is higher than 1 Hz, the GNSS-only solutions show the poorest accuracy. For frequency band 2–10 Hz, the EMD solutions show the best agreement with the reference PSD curve, since in processing the data, the noise in both the GNSS and accelerometer measurements was suppressed. The CMRKF-MA method performed better than the CMRKF method although their curves were similar in the

2–10 Hz band. The EMD and GNSS-only methods failed to detect the vibration signals of over 10 Hz, agreeing with the Nyquist frequency principle. The UMRKF-MA method offered the most consistent PSD results with the reference data across the whole frequency range, especially for the higher frequency band (zone 4: 2–100 Hz), indicating the outstanding performance of the method in both the temporal and frequency domains.
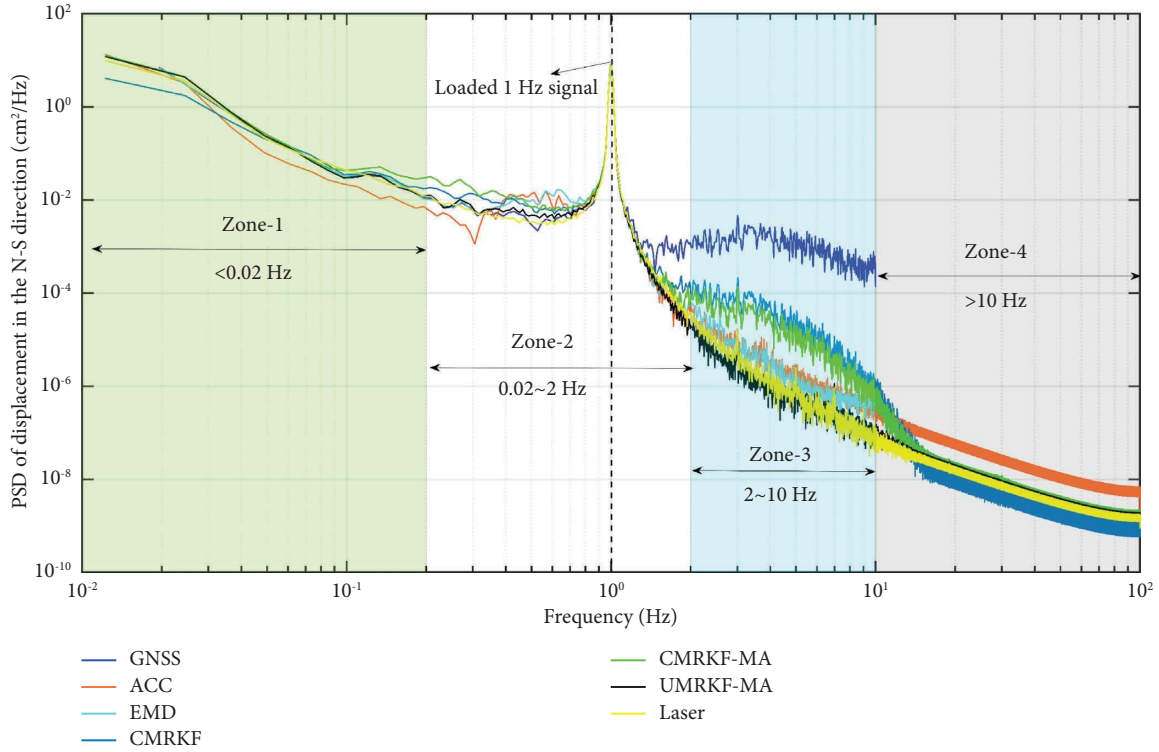
FIGURE 5: PSD results of displacements computed from the MA-GNSS, the accelerometer (ACC) measurements, the EMD-based fusion algorithm (EMD), the conventional Kalman filter (CMRKF), CMRKF-MA, and UMRKF-MA based on data from sinusoidal displacement simulation. The PSD results of the laser measurements are also given as the truth for comparison.

3.3. Experiment with Random Displacements. Similar to the test with the simulated sinusoidal displacements, the shaking table first remained static for a short period of time (about 60 s) to obtain the reference coordinates, and then random displacements were generated. The shaking table was also tilted manually when the displacements were simulated. The data sampling rates were 20 Hz for the GNSS and 200 Hz for the accelerometer and the laser transducer, respectively.

Figure 6 shows the displacement time series computed based on the six computational schemes described above. The errors in the displacements relative to the laser measurements and the statistics are also given in the plots and in Table 3. The data resolutions of the GNSS and the EMD fusion solutions were 20 Hz and 200 Hz for the other solutions.

The accuracy of the GNSS-only solution (Figure 6(a)) in the random displacement test was slightly lower than that in the sinusoidal displacement test, with the RMSE being 2.4 mm compared with 1.5 mm in the case of the sinusoidal displacement test. Part of the low-frequency errors in the accelerometer measurements was removed by the high-pass filter. The ACC solutions (Figure 6(b)) still had high peak error and RMSE, 21.7 mm and 12.2 mm, respectively. The tilt angle of the shaking table impacted significantly the CMRKF solutions (Figure 6(d)), resulting in high peak error and RMSE, 32.6 mm and 12.7 mm, respectively. The denoising capability of the EMD helped reduce the effect of the misalignment errors and achieve an accuracy that is compatible with that of the GNSS data-only solutions

(RMSE = 2.7 mm). After correcting the misalignment errors of the accelerometer with the MA-GNSS observations, both CMRKF-MA and UMRKF-MA produced improved results. Compared to the results of CMRKF, the RMSE and peak error of CMRKF-MA were reduced by about 83% and 73% to 2.2 mm and 9.1 mm, respectively. UMRKF-MA further improved the accuracy by about 35%.

Welch's PSDs of the computed displacements from the different computation schemes are given in Figure 7. The results show that the different computational schemes produced largely similar PSDs in the low frequency (lower than 0.1 Hz) and high frequency (higher than 15 Hz) bands. The major differences in the PSDs between the different computational schemes are in the 2–10 Hz frequency band, where the PSD of the UMRKF-MA is similar to that of the EMD and is better than that of the CMRKF and CMRKF-MA. For frequency bands higher than 10 Hz, the CMRKF-MA and UMRKF-MA performed the best, indicating the effectiveness of the proposed method of using the MA-GNSS data to correct the misalignment errors.

4. Tests with Data from a Long-Span Bridge under Heavy Vehicle Loading

Stonecutters Bridge (SCB) is a long-span cable-stayed bridge in Hong Kong that was constructed during 2004–2012 and is the third-longest cable-stayed bridge in the world. As shown in Figure 8(a), SCB is supported by eight piers, and two 298-meter-tall cable towers, and has a main span of 1080 meters
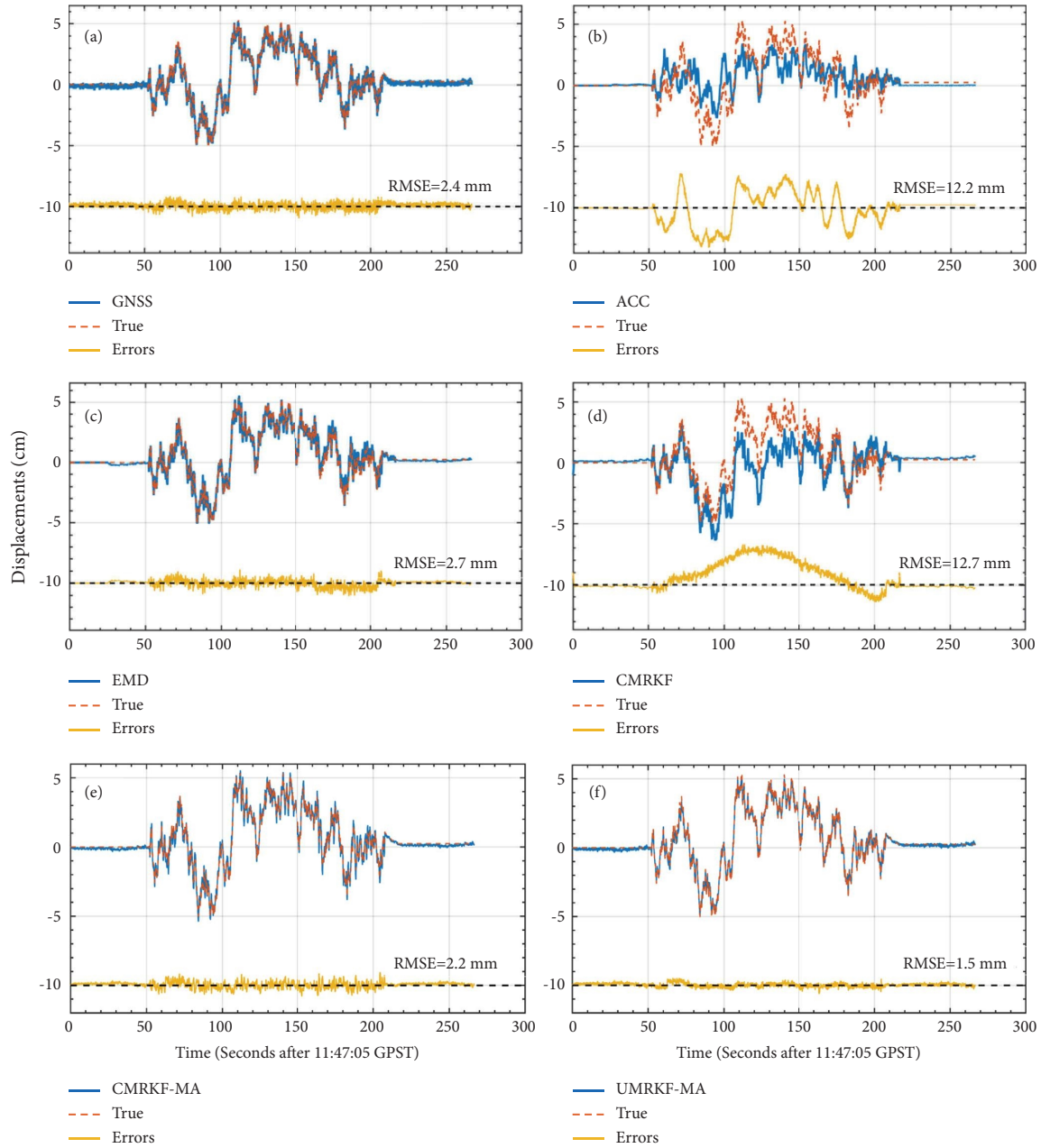
FIGURE 6: Displacements computed and their errors for the test with the simulated random displacements. (a) GNSS data only. (b) Integration from accelerometer data after a high-pass filter. (c) GNSS and accelerometer data fusion with EMD. (d) GNSS and accelerometer data fusion with CMRKF. (e) GNSS and accelerometer data fusion with CMRKF-MA. (f) GNSS and accelerometer data fusion with UMRKF-MA.

TABLE 3: Statistics of displacement errors based on the six computation schemes for the random displacement test (unit: mm).

Computation schemes	GNSS	ACC	EMD	CMRKF	CMRKF-MA	UMRKF-MA
Peak error	8.9	21.7	11.3	32.6	9.1	5.8
RMSE	2.4	12.2	2.7	12.7	2.2	1.5

and two side spans of 289 meters. A long-term SHM system, including GNSS, accelerometers, and thermometers, was deployed to monitor the health conditions of the bridge. The SHM data from the SCB under vehicle loadings were used to demonstrate the advantage of the proposed method. The

SHM system has eight pairs of colocated GPS receivers and accelerometers installed on the towers and the deck of the bridge as shown in Figure 8(b). The raw displacements (denoted as GPS solutions hereinafter) were calculated using the RTK technique and multi-GNSS data (GPS: L1/L2 and
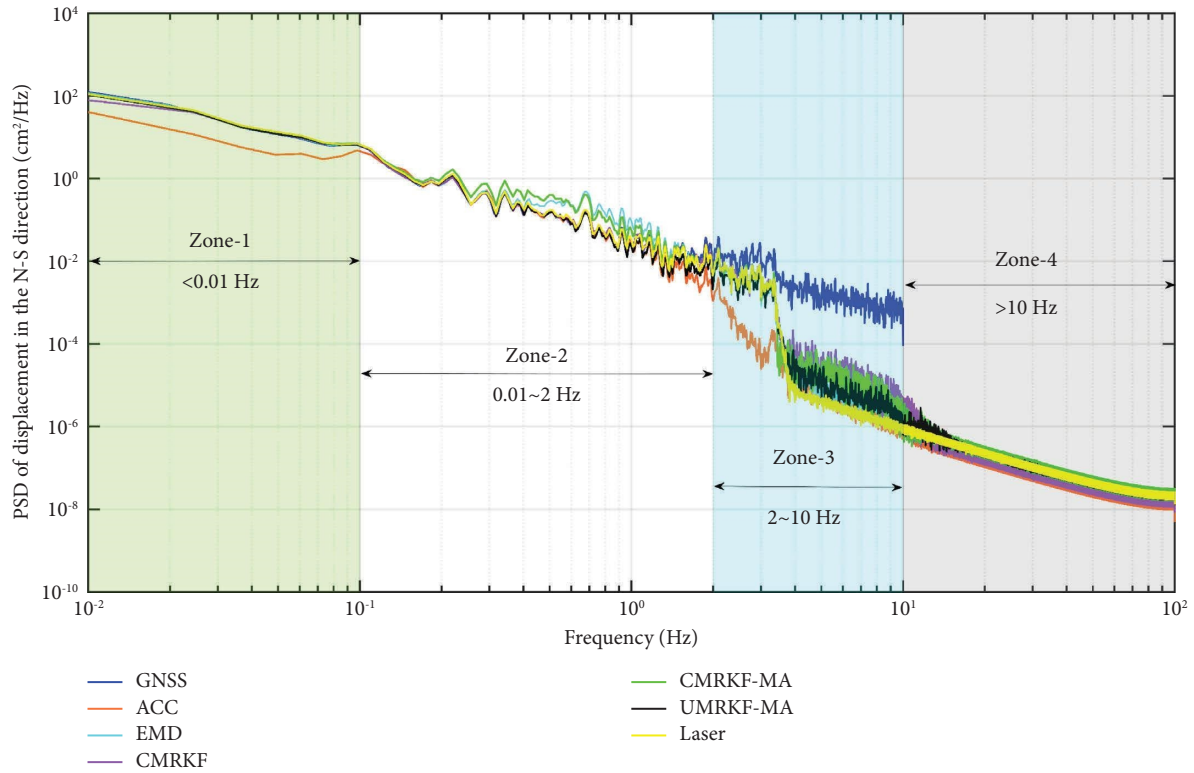
Figure 7: PSDs of displacements from the laser transducer, the multi-antenna GNSS, the accelerometer (ACC), the EMD-based fusion algorithm (EMD), the conventional multi-rate Kalman filter (CMRKF), CMRKF-MA, and UMRKF-MA for the random displacement test.

GLONASS: G1/G2) from Leica GRX1230GG GNSS receivers acquired at a sampling rate of 10 Hz. The distance between reference (at the Nam Wan end of the bridge) and monitoring stations is about 1.5 km.

Monitoring data during a heavy vehicle loading test were collected at a sampling rate of 10 Hz for the GNSS data and 50 Hz for the accelerometers. The bridge was temporarily closed to the public during the test and a convoy of trucks with a total weight of nearly 500 tons first assembled at the west tower (Figure 8(a)) and then moved together eastwards along the bridge (Figure 8(b)) to generate the loadings to the bridge. A similar test was then done when the vehicles moved westwards. Figure 9 shows the 3D displacement and acceleration signatures at the GPS-2/ACC-2 station (Figure 8(b)) during the test. The most significant displacements occurred at the station in the vertical direction, with the maximum vertical displacement reaching −100 mm and −150 mm, respectively, during the two time periods of vehicle loadings. The vehicle induced a longitudinal displacement of less than 20 mm and no obvious transversal displacement. The acceleration response showed a similar pattern although also indicated some acceleration in the transversal direction of the bridge.

Figure 10 shows the transverse displacements derived from data of GPS-2, the fusion of GPS-2 and ACC-2 data with MRKF, and the fusion of GPS-2, GPS-3, and ACC-2 data with UMRKF-MA. It should be noted that we have assumed that the structure between GPS-2 and GPS-3 was a rigid body and a two-antenna MA system was formed by
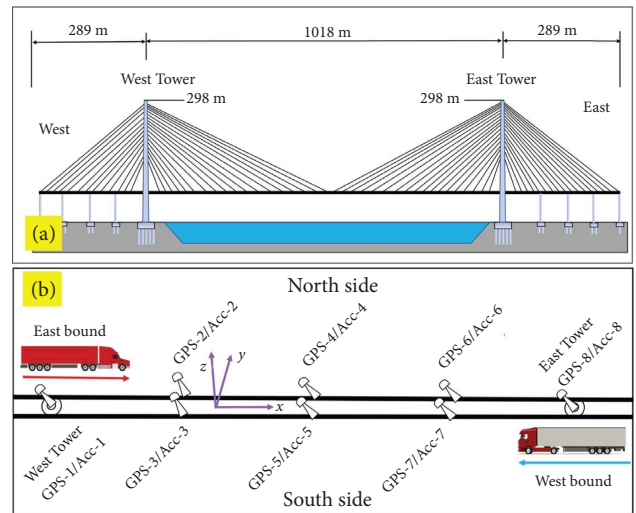

Figure 8: (a) Configuration of SCB and (b) layout of colocated GPS and accelerometers. The bridge reference system is given in blue lines.

the two antennas when using the UMRKF-MA model. It can be found in Figure 10 that the displacements computed with UMRKF-MA agree well with those computed with GPS data alone, but the noise level in the former was much lower. The displacements from the MRKF were significantly different from the other two solutions over the time periods of vehicle loading as highlighted with the red dashed rectangles. The
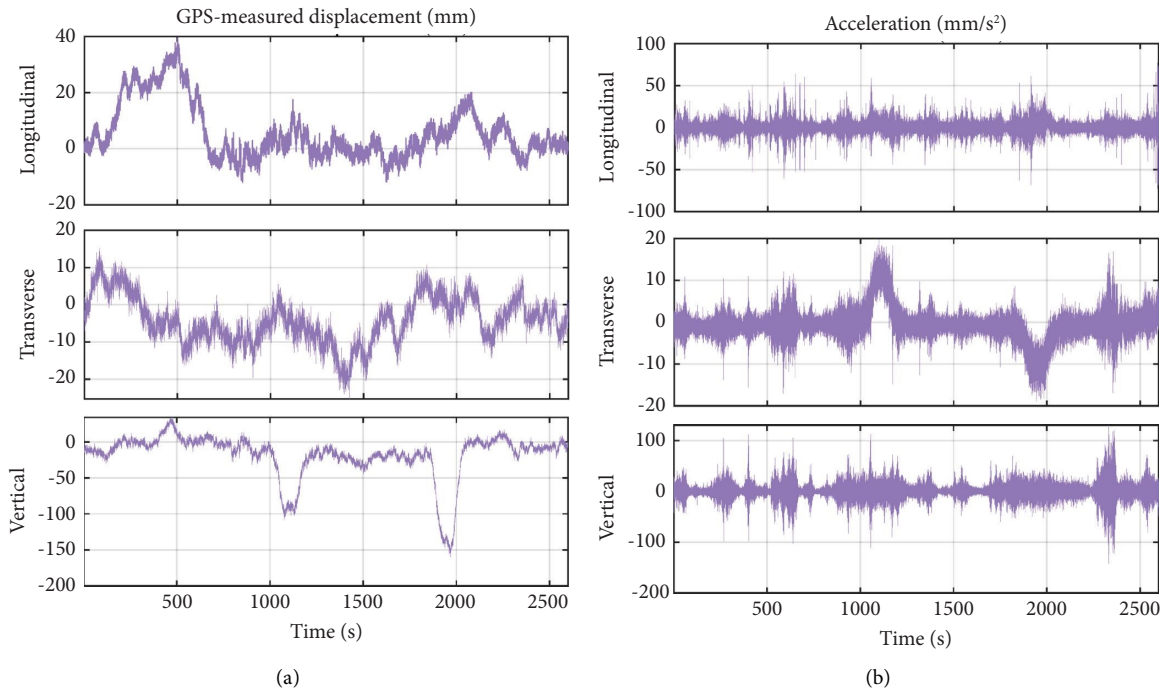
(a)

(b)

FIGURE 9: Displacements (a) and accelerations (b) at station GPS-2/ACC-2 in the longitudinal (top panel), transversal (mid-panel), and vertical (bottom panel) directions of the bridge, respectively.
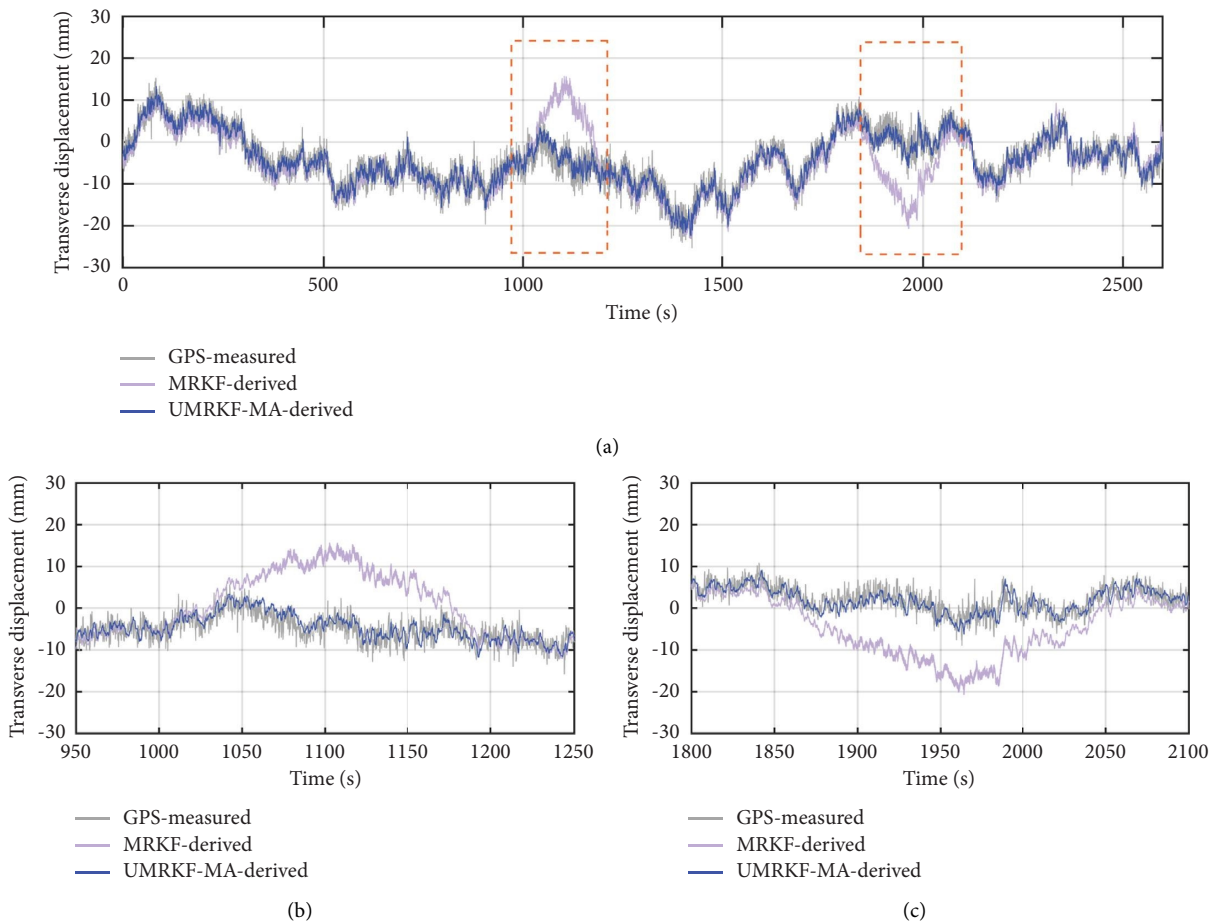

(a)

(b)

(c)

FIGURE 10: (a) Transverse displacements computed from GPS-2 data (gray lines), fusion of GPS-2 and ACC-2 with MRKF (light blue lines), and data fusion of GPS-2, GPS-3, and ACC-2 with UMRKF-MA (blue lines), respectively. (b) and (c) are enlarged plots of the two sections highlighted in (a).
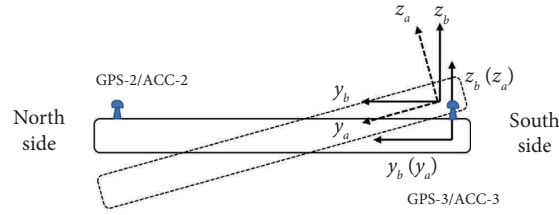
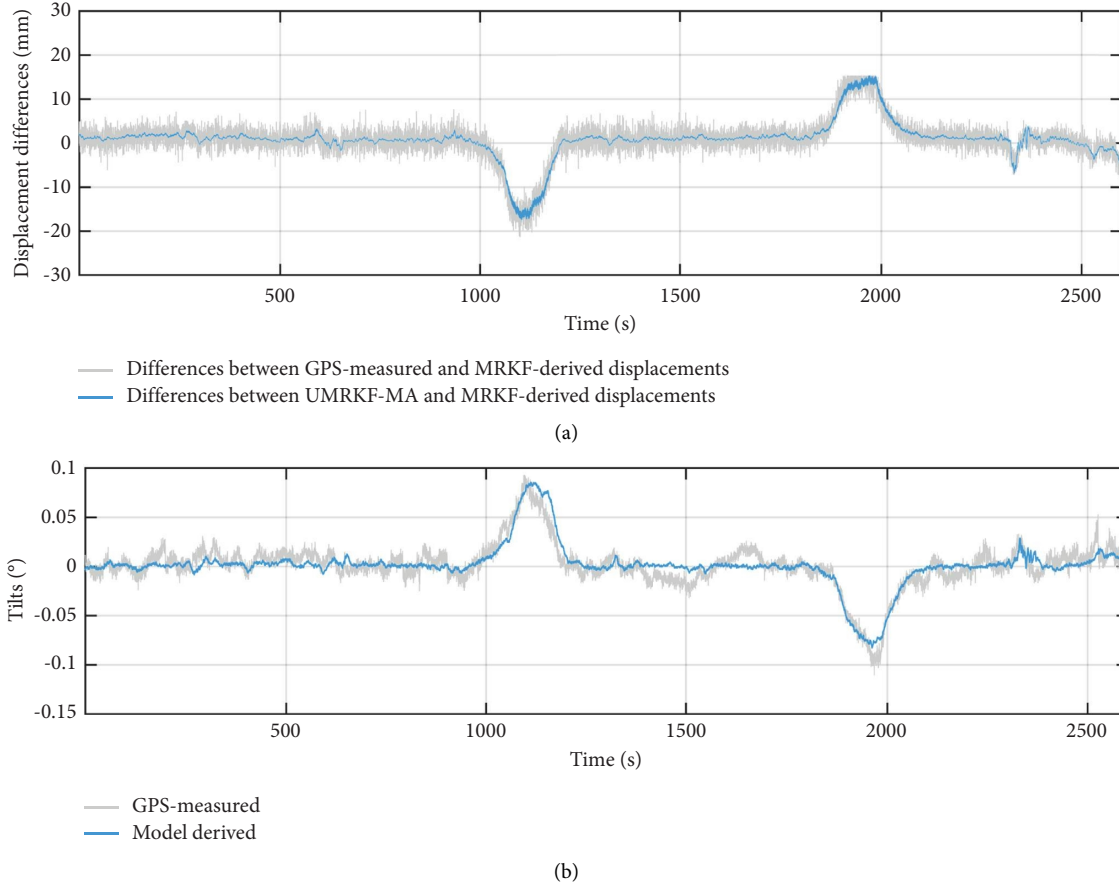FIGURE 11: Bridge deck cross section at GPS-2 and GPS-3.

(a)

(b)

FIGURE 12: (a) Differences between the displacements computed with the fusion of GPS-2 and ACC-2 data with MRKF and from GPS-2 data only and between the MRKF-derived displacements and those computed from the fusion of GPS-2, GPS-3, and ACC-2 data with UMRKF-MA, all for GPS-2 station. (b) Tilt angles of the bridge deck at GPS-2 station computed from MA-GPS observations and from estimation using the UMRKF-MA.

MRKF model may have overestimated the transverse displacements by up to over 10 mm as shown in Figures 10(b) and 10(c). The likely reason for the results was that when the vehicle loading was applied on one side of the bridge deck, the loading caused the bridge deck to tilt about the x-axis (or a line parallel to the x-axis), resulting in the misalignment between the BRF and the ARF. As shown in Figure 11, when the bridge deck was tilted about the x-axis, part of the accelerations in the vertical direction was transformed into the transverse direction, affecting the computed transverse displacements (Figures 9 and 10).

We have calculated the tilt angles of the bridge deck and the displacement differences between the MRKF-derived and the GPS-measured results and between the MRKF-derived and UMRKF-MA-calculated results, respectively, as shown in Figure 12. For the computation of the former,

the MRKF-derived displacements were first downsampled to 10 Hz, the same as that of the GPS measurements. The difference in the displacements between the MRKF-derived results and the results of the other two solutions had a strong correlation with the calculated tilt angle, which again verified that the misalignment error in the MRKF displacements was due to the tilt of the bridge deck.

5. Conclusions

We have proposed a new method for integrating data from a multi-antenna GNSS and an accelerometer with an unscented multi-rate Kalman filter (UMRKF-MA) to correct the system misalignment errors between the sensors and to produce much higher accuracy real-time displacement measurements for monitoring structural health conditions of large civil infrastructures. Experimental results with displacement data simulated with a shaking table and from a loading test of a large cable-stayed bridge indicated that the misalignment errors have significant effects on the fusion results, resulting in the overestimation of displacement with a magnitude of nearly 2 cm. The proposed method was effective in correcting the misalignment errors and that the accuracy of real-time displacement measurements could be improved by up to about 40% over using a standard RTK GNSS approach and by up to about 65% over integrating the multi-antenna GNSS and accelerometer data using conventional multi-rate Kalman filter method without considering the misalignment errors, and that about 1 mm level of real-time monitoring of displacements could be realized using the new method. We recommend strongly to consider the misalignment errors between accelerometers and GNSS when integrating the observations in monitoring all major civil infrastructures that may experience significant displacements to maximize the accuracy and reliability of such structural health monitoring systems.

Data Availability

The datasets used in this study are available from the corresponding author on reasonable request.

Conflicts of Interest

The authors declare that they have no conflicts of interest.

Authors' Contributions

XYQ designed the research, developed the approach, performed the experiment, analyzed the data, and wrote the manuscript. XLD designed the research, analyzed the data, and wrote and revised the manuscript. YLX and WKY analyzed the data and revised the manuscript. All authors reviewed the manuscript.

Acknowledgments

References

[1] N. J. Gardner, J. Huh, and L. Chung, "Lessons from the Sampoong department store collapse," *Cement and Concrete Composites*, vol. 24, no. 6, pp. 523–529, 2002.

[2] J. Yu, X. Meng, B. Yan, B. Xu, Q. Fan, and Y. Xie, "Global Navigation Satellite System-based positioning technology for structural health monitoring: a review," *Structural Control and Health Monitoring*, vol. 27, no. 1, p. e2467, 2020.

[3] D. W. Zheng, P. Zhong, X. L. Ding, and W. Chen, "Filtering GPS time-series using a Vondrak filter and cross-validation," *Journal of Geodesy*, vol. 79, no. 6-7, pp. 363–369, 2005.

[4] C. Xue and P. A. Psimoulis, "Monitoring the dynamic response of a pedestrian bridge by using low-cost GNSS receivers," *Engineering Structures*, vol. 284, Article ID 115993, 2023.

[5] W. Yu, H. Peng, L. Pan, W. Dai, X. Qu, and Z. Ren, "Performance assessment of high-rate GPS/BDS precise point positioning for vibration monitoring based on shaking table tests," *Advances in Space Research*, vol. 69, no. 6, pp. 2362–2375, 2022.

[6] Q. Xia, W. L. Wu, F. N. Li et al., "System design and demonstration of performance monitoring of a butterfly-shaped arch footbridge," *Structural Control and Health Monitoring*, vol. 28, no. 7, Article ID e2738, 2021.

[7] H. A. Msaewe, P. A. Psimoulis, C. M. Hancock, G. W. Roberts, and L. Bonenberg, "Monitoring the response of Severn Suspension Bridge in the United Kingdom using multi-GNSS measurements," *Structural Control and Health Monitoring*, vol. 28, no. 11, Article ID e2830, 2021.

[8] W. Yu, X. Ding, W. Dai, and W. Chen, "Systematic error mitigation in multi-GNSS positioning based on semi-parametric estimation," *Journal of Geodesy*, vol. 91, no. 12, pp. 1491–1502, 2017.

[9] P. Zhong, X. Ding, L. Yuan, Y. Xu, K. Kwok, and Y. Chen, "Sidereal filtering based on single differences for mitigating GPS multipath effects on short baselines," *Journal of Geodesy*, vol. 84, no. 2, pp. 145–158, 2010.

[10] F. Moschas and S. Stiros, "PLL bandwidth and noise in 100 Hz GPS measurements," *Global Positioning System Solutions*, vol. 19, no. 2, pp. 173–185, 2015.

[11] X. Qu, B. Shu, X. Ding, Y. Lu, G. Li, and L. Wang, "Experimental study of accuracy of high-rate GNSS in context of structural health monitoring," *Remote Sensing*, vol. 14, no. 19, p. 4989, 2022.

[12] X. Li, L. Ge, E. Ambikairajah, C. Rizos, Y. Tamura, and A. Yoshida, "Full-scale structural monitoring using an integrated GPS and accelerometer system," *Global Positioning System Solutions*, vol. 10, no. 4, pp. 233–247, 2006.

[13] X. Y. Qu, X. Ding, Y. L. Xu, and W. Yu, "Real-time outlier detection in integrated GNSS and accelerometer structural health monitoring systems based on a robust multi-rate Kalman filter," *Journal of Geodesy*, vol. 97, no. 4, pp. 38–18, 2023.

[14] G. W. Roberts, X. Meng, and A. H. Dodson, "Integrating a global positioning system and accelerometers to monitor the deflection of bridges," *Journal of Surveying Engineering*, vol. 130, no. 2, pp. 65–72, 2004.

[15] C. Hide, S. Blake, X. Meng, G. Roberts, T. Moore, and D. Park, "An Investigation in the use of GPS and INS sensors for structural health monitoring," in *Proceedings of the 18th International Technical Meeting of the Satellite Division of The Institute of Navigation (ION GNSS 2005)*, pp. 2029–2038, September 2005.

[16] W. S. Chan, Y. L. Xu, X. L. Ding, and W. J. Dai, "An integrated GPS–accelerometer data processing technique for structural deformation monitoring," *Journal of Geodesy*, vol. 80, no. 12, pp. 705–719, 2006.

[17] F. Moschas and S. Stiros, "Measurement of the dynamic displacements and of the modal frequencies of a short-span pedestrian bridge using GPS and an accelerometer," *Engineering Structures*, vol. 33, no. 1, pp. 10–17, 2011.

[18] T. H. Yi, H. N. Li, and M. Gu, "Experimental assessment of high-rate GPS receivers for deformation monitoring of bridge," *Measurement*, vol. 46, no. 1, pp. 420–432, 2013.

[19] H. Han, J. Wang, X. Meng, and H. Liu, "Analysis of the dynamic response of a long span bridge using GPS/accelerometer/anemometer under typhoon loading," *Engineering Structures*, vol. 122, pp. 238–250, 2016.

[20] A. Smyth and M. Wu, "Multi-rate Kalman filtering for the data fusion of displacement and acceleration response measurements in dynamic system monitoring," *Mechanical Systems and Signal Processing*, vol. 21, no. 2, pp. 706–723, 2007.

[21] X. Meng, J. Wang, and H. Han, "Optimal GPS/accelerometer integration algorithm for monitoring the vertical structural dynamics," *Journal of Applied Geodesy*, vol. 8, no. 4, pp. 265–272, 2014.

[22] J. Kim, K. Kim, and H. Sohn, "Autonomous dynamic displacement estimation from data fusion of acceleration and intermittent displacement measurements," *Mechanical Systems and Signal Processing*, vol. 42, no. 1-2, pp. 194–205, 2014.

[23] K. Kim, J. Choi, J. Chung, G. Koo, I. H. Bae, and H. Sohn, "Structural displacement estimation through multi-rate fusion of accelerometer and RTK-GPS displacement and velocity measurements," *Measurement*, vol. 130, pp. 223–235, 2018.

[24] Y. Xu, J. M. W. Brownjohn, D. Hester, and K. Y. Koo, "Long-span bridges: enhanced data fusion of GPS displacement and deck accelerations," *Engineering Structures*, vol. 147, pp. 639–651, 2017.

[25] J. Paziewski, K. Stepniak, R. Sieradzki, and C. O. Yigit, "Dynamic displacement monitoring by integrating high-rate GNSS and accelerometer: on the possibility of downsampling GNSS data at reference stations," *Global Positioning System Solutions*, vol. 27, no. 3, p. 157, 2023.

[26] J. N. Yang, S. Lin, H. Huang, and L. Zhou, "An adaptive extended Kalman filter for structural damage identification," *Structural Control and Health Monitoring*, vol. 13, no. 4, pp. 849–867, 2006.

[27] M. N. Cahyadi, T. Asfihani, H. F. Suhandri, and R. Erfianti, "Unscented Kalman filter for a low-cost GNSS/IMU-based mobile mapping application under demanding conditions," *Geodesy and Geodynamics*, 2023.

[28] B. Yu, L. Chen, and M. Fatin Fatihur Rahman, "Design of multi-sensor fusion positioning and navigation method based on federated kalman filter for low-speed rotorcraft of atmospheric detection journal of physics: conference series,"

[29] *Journal of Physics: Conference Series*, vol. 2428, no. 1, Article ID 012031, 2023.

[29] D. M. Boore and J. J. Bommer, "Processing of strong-motion accelerograms: needs, options and consequences," *Soil Dynamics and Earthquake Engineering*, vol. 25, no. 2, pp. 93–115, 2005.

[30] C. Pan, R. Zhang, H. Luo, and H. Shen, "Baseline correction of vibration acceleration signals with inconsistent initial velocity and displacement," *Advances in Mechanical Engineering*, vol. 8, no. 10, Article ID 168781401667553, 2016.

[31] J. Geng, D. Melgar, Y. Bock, E. Pantoli, and J. Restrepo, "Recovering coseismic point ground tilts from collocated high-rate GPS and accelerometers," *Geophysical Research Letters*, vol. 40, no. 19, pp. 5095–5100, 2013.

[32] C. O. Yigit, A. El-Mowafy, A. Anil Dindar, M. Bezcioglu, and I. Tiryakioglu, "Investigating Performance of high-rate GNSS-PPP and PPP-AR for structural health monitoring: dynamic tests on shake table," *Journal of Surveying Engineering*, vol. 147, no. 1, Article ID 05020011, 2021.

[33] P. Xu, Y. Shu, X. Niu, J. Liu, W. Yao, and Q. Chen, "High-rate multi-GNSS attitude determination: experiments, comparisons with inertial measurement units and applications of GNSS rotational seismology to the 2011 Tohoku Mw9.0 earthquake," *Measurement Science and Technology*, vol. 30, no. 2, Article ID 024003, 2019.

[34] S. Wu, X. Zhao, C. Pang, L. Zhang, Z. Xu, and K. Zou, "Improving ambiguity resolution success rate in the joint solution of GNSS-based attitude determination and relative positioning with multivariate constraints," *GPS Solutions*, vol. 24, pp. 31–14, 2020.

[35] S. J. Julier and J. K. Uhlmann, "Unscented filtering and nonlinear estimation," *Proceedings of the IEEE*, vol. 92, no. 3, pp. 401–422, 2004.

[36] G. Lu, *Development of a GPS Multi-Antenna System for Attitude Determination*, University of Calgary, Calgary, Canada, 1995.

[37] B. Zhang, X. Ding, C. Werner et al., "Dynamic displacement monitoring of long-span bridges with a microwave radar interferometer," *International Society for Photogrammetry and Remote Sensing Journal of Photogrammetry and Remote Sensing*, vol. 138, pp. 252–264, 2018.

[38] P. Rebischung, Z. Altamimi, J. Ray, and B. Garayt, "The IGS contribution to ITRF2014," *Journal of Geodynamics*, vol. 90, no. 7, pp. 611–630, 2016.

[39] S. Butterworth, "On the theory of filter amplifiers," *Wireless Engineer*, vol. 7, no. 6, pp. 536–541, 1930.

[40] P. Welch, "The use of fast Fourier transform for the estimation of power spectra: a method based on time averaging over short, modified periodograms," *IEEE Transactions on Audio and Electroacoustics*, vol. 15, no. 2, pp. 70–73, 1967.